Bending Properties of Representative Composite Aircraft Structures Under Oil Pressure

Liu Han[1,2(✉)], Hui Qi[2], Shifeng Li[1], Zhen Zhang[1], and Shaobo Gong[1]

[1] AVIC Harbin Aircraft Industry Group CO., LTD, Harbin 150066, China
348020580@qq.com

[2] College of Aerospace and Civil Engineering, Harbin Engineering University, Harbin 150001, China

Abstract. Composite structures adjacent to the fuel tank of a helicopter fuselage experience a substantial bending load created by the oil pressure. Thus, these structures may undergo considerable deformation. The present study investigated the bending characteristics of typical structures (spar cap) adjacent to the fuel tank. The spar cap specimens (under two conditions) were subjected to four-point bending, and the strength and failure mode were examined. Test results shown that all samples fractured at the middle of the curved part under Condition 1, which was consistent with the working conditions of an actual structure adjacent to the fuel tank. Progressive failure analysis was performed based two-dimensional Hashin failure for intralaminar failure model and bilinear traction separation constitutive model is adopted for interlaminar failure model. The results shown that the appearance and internal damage morphology obtained by the simulation are consistent with experimental results.

Keywords: Composite material · Four-point bending · Progressive failure · Intralaminar failure · Interlaminar failure · Bilinear traction separation constitutive model

1 Introduction

The percentage and configuration of composite parts used are important parameters indicating aircraft performance [1, 2]. Because of their high strength, design flexibility, and resistance to fatigue failure, as well as their ability to be manufactured in large integral (i.e., one-piece) parts, advanced composite materials are widely used in the integral tank structure to effectively reduce structure weight [3, 4]. Nevertheless, composites are associated with their own issues. For example, during use composite parts may occasionally experience impacts by foreign objects, such as birds, stones (on the runway), or tools (accidentally dropped during repairs). Such impacts can cause matrix cracking, delamination, fiber rupture, or other damage modes in composite structures. This damage severely affects the structural safety of an aircraft and, thus, has been extensively investigated. The residual mechanical properties (under tension, compression, and shear) of composite structures after a low-energy impact are a major current topic of research [5,

Chinese Society of Aeronautics and Astronautics: CASTYSF 2022, LNEE 972, pp. 224–234, 2023.
https://doi.org/10.1007/978-981-19-7652-0_21

6]. In addition, the structures adjacent to the fuel tank work under substantial bending loads due to fuel pressure and can deform considerably [7, 8]. Therefore, the out-of-plane bending properties of these structures and the residual bending performance after impact must be considered in the structural design.

The previous research were mainly focused on the bending of composite plate and sandwich structure. The typical structures adjacent to the fuel tank were seldom studied [9]. Luo Liang studied the compression after impact performance for T300/NY9200Z, T300/QY8911 and T700S/5228. Fracture mechanics behavior by means of mechanical numerical simulation The research results indicated that there are homologous knee points in these curves and these points which the damage mechanisms change significantly [10, 11]. Gong Xiaohui the studied low-velocity impact properties and three-point bending properties of the composite foamed-sandwich foam composites. The bending strength and stiffness of the foam sandwich composite board can be effectively improved, and the bending performance of the sandwich structure is effectively improved because of stiffeners [12]. Meng Xiangyao studied the three-point bending damage evolution and fracture mechanics behavior by means of mechanical numerical simulation [13]. The present study investigated the post-impact bending characteristics of typical structures (spar cap) adjacent to the fuel tank. The spar cap specimens (under two conditions) were subjected to four-point bending, the test results shown that it was consistent with the working conditions of an actual structure adjacent to the fuel tank under condition 1. Progressive failure analysis was performed based two-dimensional Hashin failure for intralaminar failure model and bilinear traction separation constitutive model is adopted for interlaminar failure model. The results shown that the appearance and internal damage morphology obtained by the simulation are consistent with experimental results.

2 Four-Point Bending

2.1 Structure of Test Specimens

Structures adjacent to the fuel tank experience high loads generated by the fuel pressure and, thus, can deform considerably. The out-of-plane bending properties of these structures are important considerations in the structural design of aircraft. Here, two typical structures adjacent to the tank, a spar cap and a spar web, were studied (Fig. 1).

Samples were prepared using prepregs fabricated from carbon fiber fabric and unidirectional tapes. Prepregs were plied and cured in an autoclave (SCHOLZ, Germany; diameter: 4 m, temperature departure: ±3 °C, ramp: 0–3 °C/min, cooling: 0–5 °C/min).

The spar cap layer:

- P1: $[\pm 45/0_2/ \pm 45/0_2/\pm 45_2/0_2/\pm 45/0_2/\pm 45]$ (thickness: 2.427 mm);
- P2: $[\pm 45/0_2/\pm 45_2/0/\pm 45_2/0_2/\pm 45]$ (thickness: 2.545 mm).

Please note that the first paragraph of a section or subsection is not indented. The first paragraphs that follows a table, figure, equation etc. does not have an indent, either. Subsequent paragraphs, however, are indented.

The materials used for preparation of test specimens are domestic carbon fiber fabric 5224/CF3052 and unidirectional tape 5224/U3160; the mechanical properties of these materials are shown in Table 1.

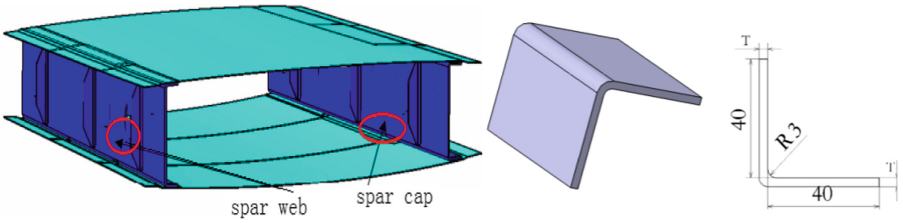

(a) wing oil tank (b) spar cap

Fig. 1. Schematic representation

Table 1. Mechanical properties of composite materials

		Unidirectional tape	Fabric
Density	(t/mm^3)	1.58e−9	1.58E−9
Longitudinal stiffness E_{11}	(GPa)	120	55
Transverse modulus E_{22}	(GPa)	9.0	55
Poisson ratio v		0.3	0.052
Shear stiffness G	(GPa)	4.1	510
Longitudinal tension strength X_T	MPa	1000	400
Transverse tension strength Y_T	(MPa)	40	500
Longitudinal compression strength X_C	MPa	700	400
Transverse compression strength Y_C	(MPa)	120	80

2.2 Spar Cap Bending Testing

Considering the spar cap deforms considerably under the bending load during operation, we tested the bending properties of this structure using a four-point bending test (ASTM D 7264) under two constraint conditions (Fig. 2). Under Condition 1 (Figs. 2a and 3a), two supporting pins (6 mm) were placed on a horizontal plane, and the distance between the pins (support span) was adjusted and fixed to 44 mm (±0.1 mm). The sample was allowed to straddle the pins, and a U-shaped loading head was inversely placed on the sample. The head contacted the sample via its round ends (6.0 ± 0.1 mm). Then a compressive load was applied at 7.5 m/min, and the sample was allowed to flatten and widen freely. Under Condition 2 (Figs. 2b and 3a), two protruding bars were engineered on the plane to prevent the sample from widening during compression; other parameters were identical to Condition 1.

Table 2 shown that all samples fractured at the middle of the curved part under Condition 1, which was consistent with the working conditions of an actual structure adjacent to the fuel tank. Under Condition 2, most samples failed at the regions contacting the loading head, exhibiting a local shearing failure mode. This was inconsistent with the out-of-plane bending condition experienced by a typical structure adjacent to the fuel tank.

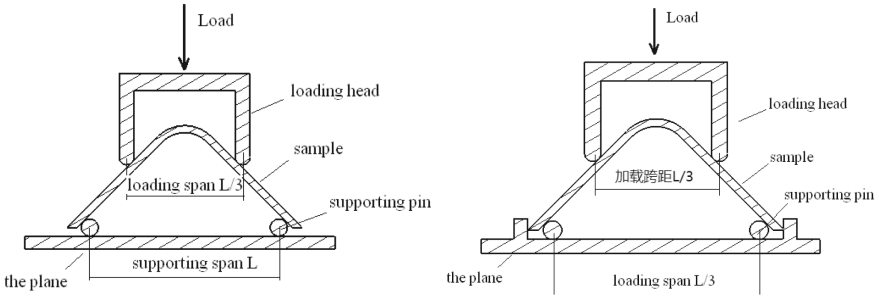

(a) Condition 1 (b) Condition 2

Fig. 2. Diagrams showing four-point bending tests

Figure 3 shown the load-displacement curve at condition 1, and Fig. 4 shown the load-displacement curve at condition 2. It can be seen that the samples exhibited only one failure mode under Condition 2: local shearing failure at the loading head-sample contact region, and the load at failure was 4–5 times higher than those tested under Condition 1 (out-of-plane bending). Additionally, comparison of results obtained from different ply arrangements (P1 versus P2) indicates that increasing the proportion of 0° plies (P1) also significantly increased the bending strength.

Table 2. Bending test results of spar cap samples

Structure		Sample code	Failure load (KN)	Displacement (mm)	Testing condition	Damage mode
Spar cap	P1	YT101	0.713	2.98	1	Fractured at the middle of the curved part
		YT102	0.784	3.21	1	
		YT103	0.798	3.04	1	
		YT104	3.270	3.61	2	Shearing failure at the regions contacting the loading head
		YT105	3.487	3.57	2	
		YT106	3.660	3.41	2	
	P2	YT201	0.732	3.82	1	Fractured at the middle of the curved part
		YT202	0.760	3.65	1	
		YT203	0.730	3.93	1	
		YT204	4.087	3.97	2	Shearing failure at the regions contacting the loading head
		YT205	4.209	3.58	2	
		YT206	3.662	4.11	2	

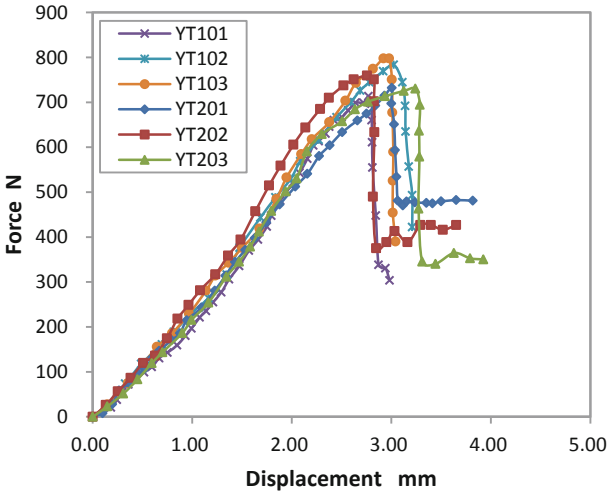

Fig. 3. Load-displacement curve at condition 1

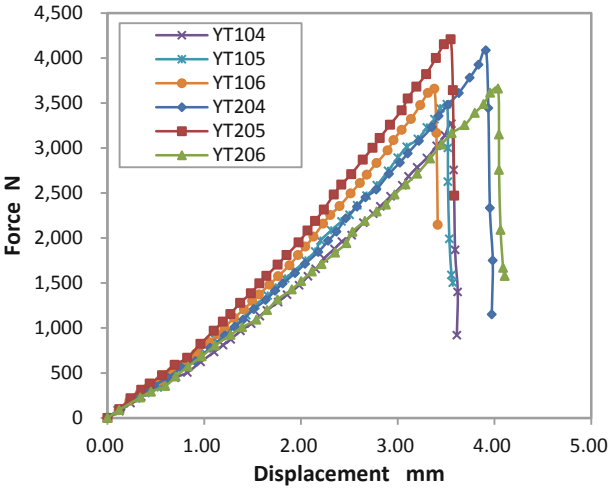

Fig. 4. Load-displacement curve at condition 2

3 Bending Failure Analysis

3.1 Interlaminar Failure Model

The damage constitutive relations of Interlaminar behavior include bilinear, trapezoid, Parabola and exponential models [14, 15]. Considering the damage of adhesive layer is elastic-brittle, the bilinear constitutive model is chosen. σ_n, σ_s and σ_t are used to describe the normal traction stress and shear stress respectively, and the stress-strain relationship of the adhesive interface behavior is [15–17]:

$$\boldsymbol{\sigma} = \mathbf{K} \cdot \boldsymbol{\delta} \tag{1}$$

where, $\mathbf{K} = [K_{nn}, K_{ss}, K_{tt}]$, $\cdot\boldsymbol{\sigma} = [\sigma_n, \sigma_s, \cdot\sigma_t]$, $\boldsymbol{\delta} = [\delta_n, \delta_s, \delta_t]$. $\mathbf{K}$ is the elastic stiffness coefficient of the adhesive interface in each stress direction, $\boldsymbol{\delta}$ is the opening displacement in each stress direction [15].

When the adhesive interface is damaged, the material shows the softening stage of damage, and the constitutive relation is [15]:

$$\boldsymbol{\sigma} = (1 - \mathbf{D})\mathbf{K} \cdot \boldsymbol{\delta} \tag{2}$$

where, $\mathbf{D}$ is the damage state variable, $\mathbf{D} = 0$, the adhesive layer is not damaged, $\mathbf{D} = 1$, which means that the adhesive is completely failure [15].

According to the description of the properties of the interface adhesive, two criteria are needed to determine the final failure of the adhesive layer [15]: The second Nominal stress Criterion (Quadratic Nominal stress Criterion) is used to determine whether the plastic layer begins to fail; B-K criterion is used to determine whether a rubber layer unit is completely failed and destroyed as the damage propagation criteria [15, 18, 19].

$$(\sigma_n/N_{\max})^2 + (\sigma_s/S_{\max})^2 + (\sigma_t/T_{\max})^2 = 1 \tag{3}$$

where, $N_{\max}, S_{\max}, T_{\max}$ are the strength of the interface in each orthogonal direction [15, 18, 19].

$$G_{IC} + (G_{IIC} - G_{IC})(G_{\text{Shear}}/G_T)^{\eta} = G_{TC} \tag{4}$$

$$G_T = G_I + G_{\text{Shear}}\,;\, G_{\text{Shear}} = G_{II} + G_{III} \tag{5}$$

where, G_{TC} is the total release energy; G_I, G_{II} and G_{III} are the fracture toughness respectively of Type I, Type II and Type III; G_I, G_{II} and G_{III} are the critical energy release rates of Type I, Type II and Type III; G_{Shear} is the shear energy release rates; the η is a constant relative to the material ($\eta = 1.45$) [15, 18, 19].

3.2 Intralaminar Failure Model

Progressive failure analysis was performed based two-dimensional Hashin failure criteria for intralaminar failure model. Four different failure models are analyzed and processed for initiation mechanism: fiber stretching (FT), fiber compression (FC), matrix stretching (MT) and matrix pressure Shrink (MC).Two-dimensional Hashin failure criteria are as follows 15 [20, 21]:

$$\begin{aligned}
FT &= \left(\hat{\sigma}_{11}/X_1^+\right)^2 + \left(\hat{\tau}_{12}/S^L\right)^2 = 1, \left(\hat{\sigma}_{11} \geq 0\right) \\
FC &= \left(\hat{\sigma}_{11}/X_1^-\right)^2 = 1, \left(\hat{\sigma}_{11} < 0\right) \\
MT &= \left(\hat{\sigma}_{22}/X_2^+\right)^2 + \left(\hat{\tau}_{12}/S^L\right)^2 = 1, \left(\hat{\sigma}_{22} \geq 0\right) \\
MC &= \left(\hat{\sigma}_{22}/2S^T\right)^2 + \left[\left(Y^c/\left(2S^T\right)\right)^2 - 1\right]\left(\hat{\sigma}_{22}/X_2^-\right) + \left(\hat{\tau}_{12}/S^L\right)^2 = 1, \left(\hat{\sigma}_{22} < 0\right)
\end{aligned} \tag{6}$$

where, X_1^+ X_1^-, X_2^+, X_2^-, S^L and S^T are longitudinal tensile strength, longitudinal compressive strength, and transverse tensile strength, transverse compression strength, longitudinal shear strength and transverse shear strength. $\hat{\sigma}_{11}$, $\hat{\sigma}_{22}$ and $\hat{\tau}_{12}$ is the component of the effective stress tensor along the fiber direction, the transverse stress and in-plane shear stress., which can be calculated from the real stress $\boldsymbol{\sigma}$ and damage parameters M [15, 20, 22].

$$\hat{\boldsymbol{\sigma}} = \mathbf{M} \cdot \boldsymbol{\sigma} \tag{7}$$

$$\mathbf{M} = \begin{bmatrix} 1/(1-d_f) & 0 & 0 \\ 0 & 1/(1-d_m) & 0 \\ 0 & 0 & 1/(1-d_s) \end{bmatrix} \tag{8}$$

where, d_f, d_m and d_s are damage variables related to fiber, matrix and shear damage respectively. Typical curves of linear evolution were used for damage.

3.3 Numerical Simulation Results

The three-dimensional numerical simulation finite element model is established according to the size of the experimental specimen (shown in Fig. 1). The width of cap was 50 mm, and the two lengths of the angel clip were 40 mm. SC8R elements were used to simulation the fabric and unidirectional tape. The loading stick and supporting roller were simulated by the S4R shell elements and the loading stick and supporting roller were in contact with the upper surface and under surface of the specimen by Penalty function (Fig. 5). Cohesive interface contact behavior was defined to simulate the intralaminar failure model. The cohesive interface parameters of the adhesive bonding interface are shown in Table 3.

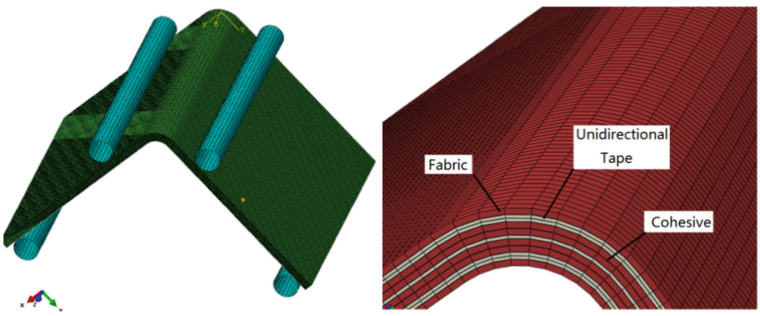

Fig. 5. Finite element model of bending failure analysis

Figure 6 shown the damage photographs under condition 1. Figure 7 shown the Different failure modes: matrix tensile failure, matrix compression failure, fiber tensile failure and fiber compression failure under condition1. It can be seen that all samples fractured at the middle of the curved part. In the simulation, the load was applied and

Table 3. Cohesive interface parameters [15]

σ_n/ MPa	σ_s/ MPa	σ_t/ MPa	K_{nn}/ N/mm^3	K_{ss}/ N/mm^3	K_{tt}/ N/mm^3	G_I/ mJ/mm^2	G_{II}/ mJ/mm^2	G_{III}/ mJ/mm^2
22	30	30	2.25e7	2.25e7	2.25e7	0.301	1.139	1.139

increased incrementally, up to an ultimate load of about 800 N. This was higher than the failure load measured experimentally, and the displacement is lower than load measured experimentally.

Figure 8 shown the load-displacement curves comparison between bending test and numerical simulation of four points bearing under condition 1.The results shown that the appearance and internal damage morphology obtained by the simulation were consistent with experimental results.

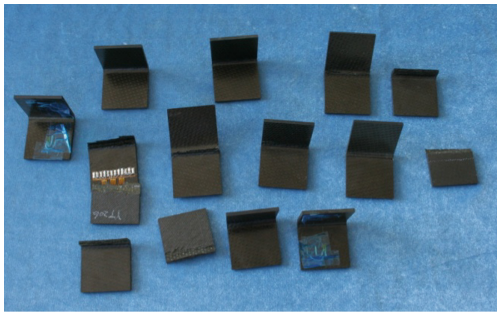

Fig. 6. The damage photographs under condition 1

4 Conclusions

Representative composite structures adjacent to the fuel tank were studied for failure mode and strength under out-of-plane bending. Based on the results, the following conclusions are drawn:

(1) The bending strengths of the spar cap samples were tested under two experimental conditions. Under Condition 2 (constrained lateral widening), the loading head caused local shearing failure, not satisfactorily simulating the loading pattern of this structure during actual use in an aircraft (out-of-plane bending by fuel pressure).
(2) Progressive failure analysis was performed based two-dimensional Hashin failure for intralaminar failure model and bilinear traction separation constitutive model was adopted for interlaminar failure model.

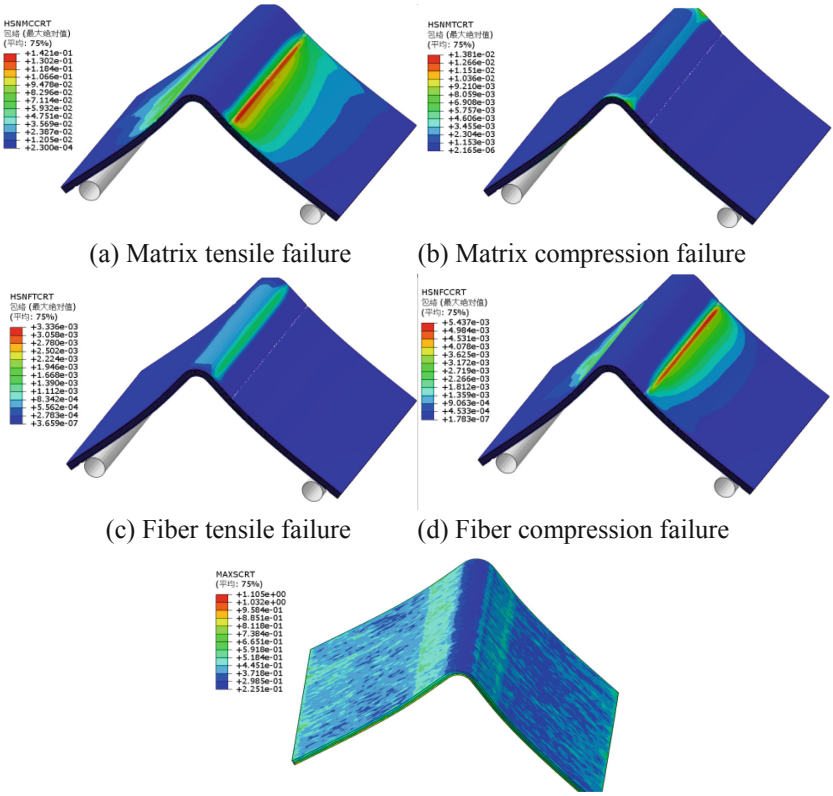

(a) Matrix tensile failure (b) Matrix compression failure

(c) Fiber tensile failure (d) Fiber compression failure

(e) Cohesive failure

Fig. 7. Load-displacement curve at condition 2

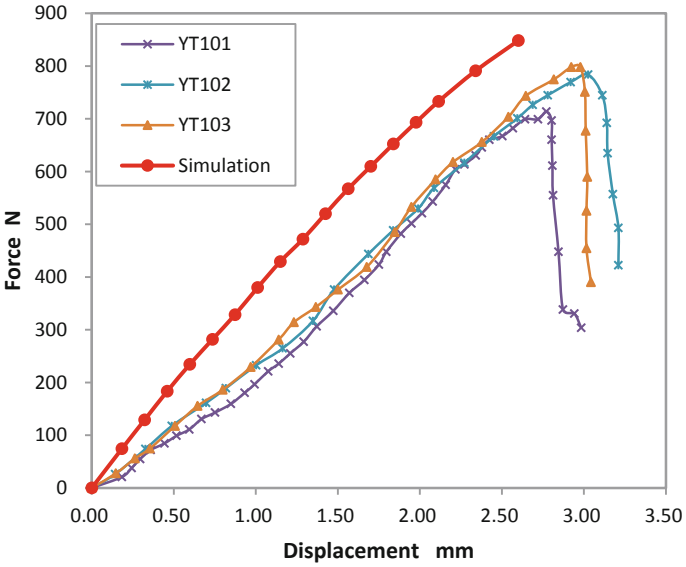

Fig. 8. Load-displacement curve at condition 2

References

1. Zhen, S., et al.: Handbook of Composite Structural Design. Aviation Industry Press, Beijing (2001)
2. Qusen, Z., et al.: Handbook of Advanced Composites. China Machine Press, Beijing (2001)
3. Lin, L.: Protection design of lightning and static of composite integral fuel tank for large civil aircraft. Civil Aircr. Design Res. **1**, 29–33 (2019)
4. Xinglong, H.: Analysis on Composite Wing Fuel Tank Seal Deformation. Nanjing University of Aeronautics and Astronautics, Nanjing (2013)
5. Serge, A.: Impact on laminate composite materials. Appl. Mech. Rev. **44**(4), 155–190 (1991)
6. Richardson, M., Wisheart M.J.: Review of low-velocity impact properties of composite material. Composites: Part A 27A, 1123–1131 (1996)
7. Xianggui, T.: Seal Failure Analysis and Test Verification on the Integral Fuel of Composite Wing. Naning University of Aeronautics and Astronautics, Nanjing (2018)
8. Jianbiao, G.: Research on composite fuel tank access door for civil aircraft. Civil Aircr. Design Res. **27**(2), 114–116 (2017)
9. Rui, X.: Sealing Performance Analysis and Structural Optimum Design of Composite Integral Fuel Tank. Naning University of Aeronautics and Astronautics, Nanjing (2017)
10. Liang, L., Zhen, S., Naichun, Y., et al.: Experimental study on low-velocity impact performance of carbon fiber reinforced composite laminates. Acta Mater. Compos. Sin. **25**(3), 20–24 (2008)
11. Shokrieh, M.M., Torabizadeh, M.A., Fereidoon, A.: Progressive failure analysis of glass/epoxy composites at low temperatures. Strength Mater. **44**(3), 134–324 (2012)
12. Xiaohui, G.: Study on Low-Velocity Impact and Bending Property of Foam Sandwich Structure. Nanchang University, Nanchang (2018)
13. Xiangyao, M., Wanpeng, D.: Damage behavior analysis of vehicle composite laminates under bending load. Agri. Equip. Veh. Eng. **59**(11), 123–126 (2021)

14. Kaixue, Y.: Investigation on Compression Strength of Honeycomb Sandwich Structure with Closing Frame. Nanchang University (2019)
15. Han, L., Qi, H., Li, R., Liu, P., Li, S., Zhan, Z., Wang, J.: Research on typical joint technology of composite stiffened skin-fuselage frame. In: Proceedings of the 5th China Aeronautical Science and Technology Conference: Lecture Notes in Electrical Engineering (2022)
16. Camanho, P., Dávila, C.: Mixed-mode decohesion finite elements for the simulation of delamination in composite materials. NASA Report, 9–12 (2002)
17. Camanho, P.P., Davila, C.G., de Moura, M.F.: Numerical simulation of mixed-mode progressive delamination in composite materials. J. Compos. Mater. **37**(16), 1415–1438 (2003)
18. Lan, J.: Research on Progressive Damage and Bonding Repair of Perforated Composite Laminates. Wuhan University of Technology, Wuhan, pp. 14–18 (2019)
19. Liang, Z., Yan, Y., Zhang, T., et al.: Experimental investigation and numerical simulation of composite laminate adhesively bonded single-lap joints. J. Beijing Univ. Aeronaut. Astronaut. **40**(12), 1786–1792 (2014)
20. Schwab, M., Todt, M., Wolfahrt, M., Pettermann, H.E.: Failure mechanism based modeling of impact on fabric reinforced composite laminates based on shell elements. Compos. Sci. Technol. **128**, 131–137 (2016)
21. Chang, F.K., Springer, G.S.: The strengths of fiber reinforced composite beads. J. Compos. Mater. **20**(1), 30–45 (1986)
22. Benzeggagh, M.L., Kenane, M.: Measurement of mixed-mode delamination fracture toughness of unidirectional glass/epoxy composites with mixed-mode bending apparatus. Compos. Sci. Technol. **56**(4), 439–449 (1996)